2D analytical airgap field model of an inset permanent magnet synchronous machine, taking into account the slotting effect

Olivier de La Barrière, Hamid Ben Ahmed, Mohamed Gabsi, Martino Lobue

2D analytical airgap field model of an inset permanent magnet synchronous machine, taking into account the slotting effect

O. de la Barrière, H. Ben Ahmed, M. Gabsi, M. LoBue

SATIE, ENS Cachan, CNRS, UniverSud
61 av du President Wilson, F-94230 Cachan, France

In this paper, an analytical method for the computation of the electromagnetic field in the airgap of an inset permanent magnet synchronous machine is proposed. The originality lies in the fact that both the stator and rotor saliencies have been taken into account in the analytical procedure. The purpose in to compute both quickly and accurately the magnetic fluxes and instantaneous torque of the machine, in order to minimize torque ripples in an optimal pre-design process. It is shown that the instantaneous torque is in good agreement with finite element results, for a shorter computation time. The model presented here can be used when the 2D approximation of the machine is valid, which is the case for most of machines' topologies.

***Index Terms*—analytical modeling, torque calculation, airgap flux, finite element verification.**

I. Introduction

ELECTRIC MOTORS for electric and hybrid traction applications have received a lot of interest in recent years [1][2][3][4], due to the necessity of reducing fuel consumption, both for economic and environmental reasons. Permanent magnet synchronous machines are promising in these demanding applications, because of their potential high torque density and efficiency [5]. The design of the electric machine for such embedded application can be difficult, due to the necessity of reaching both a high torque density and a compact size, which are contradictory optimization criteria [6] [7]. The torque quality, i.e. small torque ripple, is also an important parameter in such applications [8].

The torque ripple computation is by no way an obvious problem. Most authors use the well known finite element method [9] [10]. This method presents the advantage of taking into account all the geometrical complexity of the machine, as well as magnetic saturation. However, the computation time can be prohibitive in a first design optimization process, since the instantaneous torque computation requires a time-stepping analysis [11]. Therefore, to include the cogging torque minimization criteria in the pre-design optimization process, it is better to develop an analytical approach [12]. Most of the analytical approaches proposed in the literature are done for surface mounted permanent magnet machines [13]. However, more complex permanent magnet rotor topologies, such as the inset permanent magnet structure, can be more suitable for high speed and flux weakening purpose [14].

This article proposes an exact analytical computation of the magnetic field in the airgap of a synchronous permanent magnet machine having an inset permanent magnet topology. The double saliency of the machine (i.e. the stator slotting and the rotor ferromagnetic teeth) is taken into account analytically. In a first part, a literature review on the subject is proposed. Then the analytical model is presented, with the detailed mathematical procedure. To finish, some results about the airgap induction and instantaneous torques are given and compared with finite element analysis. A good agreement, for a much smaller computation time, has been found.

II. Overview of the previous work on the topic

The problem of modeling the stator slotting effect of electrical permanent magnet machines has been dealt with in several references of the literature. In [15], the stator slotting effect has been computed in a radial flux machine by derivation of a relative modulation function. This modulation function has been computed using the same conformal map than the one of Carter in his well-known paper [16]. However, this method only allows computing the airgap induction radial component, which is a problem for the tangential force computation by the Maxwell stress tensor method [17]. Moreover, the magnetic interaction between the slots is not taken into account. Other authors [18][19] have corrected these drawbacks of the conformal mapping method by using the numerical Schwartz-Christoffel Matlab toolbox [20], which permits to take into account rigorously the whole magnetic domain. However, this method requires the numerical computation of the conformal map coefficients, which is time consuming, because non linear transcendental equations must be solved numerically.

As an alternative to conformal mapping, some authors prefer the subdomain method [21] [22] [23], which permits to find an exact solution of the potential in the airgap of the machine, under the form of Fourier series. The idea of this method is to decompose the machine airgap into elementary rectangular domains. The Laplace or Poisson equation is solved in each domain, and the domains are linked using classical boundary conditions in electromagnetism. This method generally requires a numerical inversion of a linear Cramer system, which can be done quite easily and fastly compared to the transcendental equations of the conformal map. Some papers [21][22] apply this method to the rotor saliency for inserted permanent magnet machines. Other authors [13], on the contrary, use this method to compute the stator slotting effect of surface mounted permanent magnet machines, which can be with a double excitation winding [24]. Other authors have even managed to take into account analytically a more complex shape for the slots than a

simple rectangular [25].
In each case, some work remains to be done to take into account both the stator slotting effect, and the salient pole rotor topology with inset magnets. This is the purpose of the further analytical development.
Thanks to the model presented in this work, it will be possible to include the torque ripple minimization criterion from early pre-design stages, without increasing too much the computation time. Indeed, the pre-design of hybrid vehicles is a hard task [26], since all the traction chain has to be taken into consideration. Thus, for computation time purposes, the model used for the actuator is often simplified. For example, in [27], the slotting effect of the machine has been neglected. This can be a problem, because the torque quality (i.e. low torque ripples) is also an important point in such applications.

III. Symplifying Hypothesis for the Analytical Modelling

A. 2D assumption and machine's topology

As done in all the previous references about analytical modeling, the machine is considered as bi-dimensional (2D), i.e. the edges effects are neglected. This means that the machine is considered as infinite perpendicularly to the plane of representation.
This is typically the case in conventional radial flux machines [19] in which the axial length H is important compared to the pole pitch characteristic dimension τ.
Notice that this 2D assumption can be also valid for others topologies than conventional radial flux machines. For example, for axial flux machines [28], the 2D assumption is also possible, provided the difference H between the external and internal radii is important compared to the pole pitch τ at the mean radius. More precisely, for an axial flux machine, it is first assumed that the electromagnetic phenomena happening at the mean radius are sufficient to describe the behavior of the machine. The machine is made equivalent to a fictitious linear actuator having the same geometry than the real axial flux machine at its mean radius. Then the thickness H of this fictitious linear actuator is assumed to be very important compared to its pole pitch τ. This 2D approximation for the axial flux machine is summed up in Fig. 1.

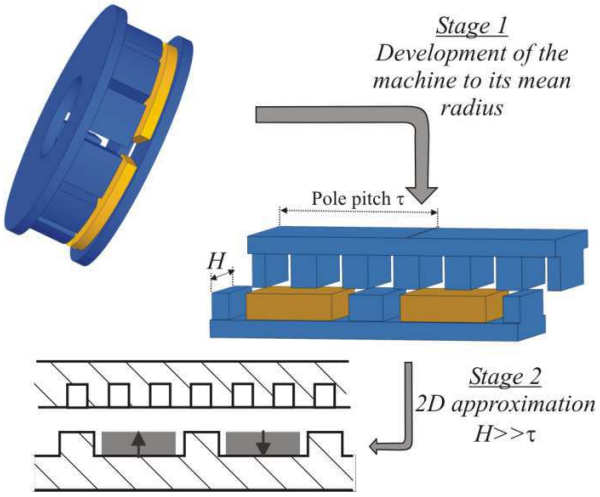

Fig. 1: 2D approximation of the axial flux machine

Then, under the 2D assumption, for both a radial and axial flux machine, the problem to study can be represented in Fig. 2 (the main geometrical parameters are given in this figure, and are recalled in Table I). For the radial flux machine, such a representation implies that the curvature of the machine has been neglected, which is valid if the mean airgap radius (i.e. the mid airgap radius) is important compared to the dimensions along the y axis. This is assumed to be the case in the following of this paper. A discussion about this simplifying assumption is given in the Appendix 1.

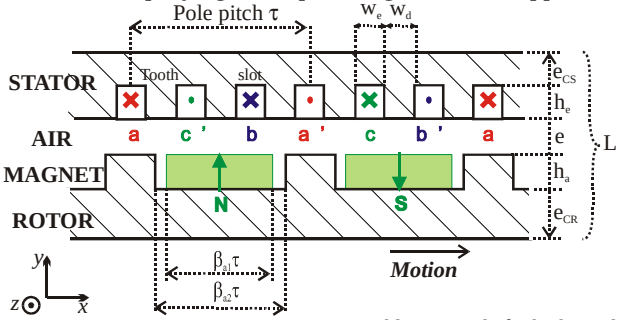

Fig. 2: 2D problem to study for both a radial and axial flux machine, and main geometrical parameters

TABLE I
GEOMETRICAL PARAMETERS OF THE MACHINE

Description	Notation
Dimensions along the *x* direction	
Pole pitch	τ
Magnet relative opening with regard to the pole pitch	β_{a1} ($0<\beta_{a1}<1$)
Rotor inter-teeth space relative opening with regard to the pole pitch	β_{a2} ($\beta_{a1}<\beta_{a2}<1$)
Stator slot width	w_e
Stator tooth width	w_d
Dimensions along the *y* direction	
Magnet thickness	h_a
Airgap width	e
Rotor yoke thickness	e_{cr}
Stator yoke thickness	e_{cs}
Slot dept	h_e
Total width of the machine	$L=e_{cr}+h_a+e+h_e+e_{cs}$
Dimensions along the *z* direction	
Active thickness of the machine along the *z* axis	H
Physical data	
Remanent induction of the magnets (*NdFeB*) at room temperature	B_r

B. Other hypothesis

Other classical simplifying assumptions are made:

– No saturation effect is taken into account. The magnetic permeability of the ferromagnetic parts is assumed to be infinite. This assumption is also discussed in Appendix I.

– It is assumed that continuous rate has been reached, and that the machine is driven with sinusoidal currents waves.

– Finally, the current density in each slot is assumed to be uniform in the entire slot surface.

IV. THE CALCULATION METHOD

A. Definition of the problem

Fig. 3 shows the machine over one pole pitch. For simplicity, the number of stator slots per pole is chosen to equal to 3.

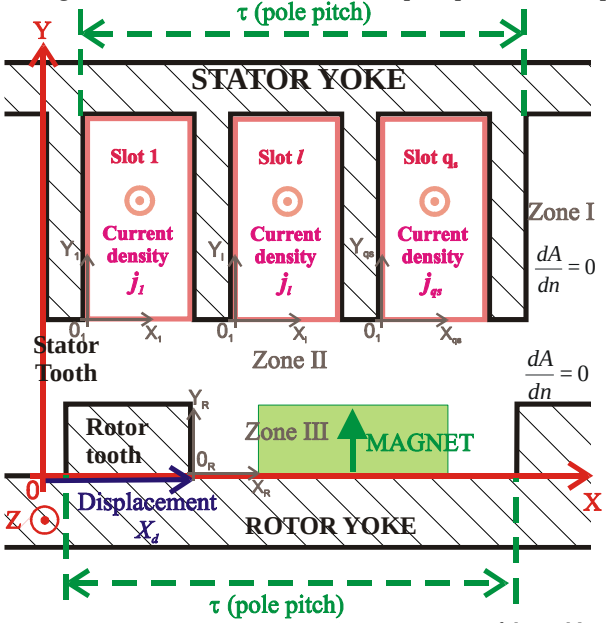

Fig. 3: Representation of the problem to solve, with double (i.e. rotor and stator) saliencies

Due to the 2D approximation, the problem can be reduced to the computation of the following vector potential:

$$\vec{A}(x,y) = A(x,y).\vec{u}_z \qquad (1)$$

Each slot is characterized by a number *l*, where *l* can evolve between 1 and 3. The current density in the slot *l* is called j_l, and is assumed to be uniform over the slot. A first difficulty arises from the fact that the geometry of the problem and its solution depend on the rotor displacement X_d. The stator slots zone is called Zone I, the airgap is called Zone II, and Zone III is the magnet zone (Fig. 3).

B. Vector potential mathematical expressions

In Zone III, due to the magnet (whose magnetization function is called *M(x)*), the potential is given by a Poisson equation:

$$\Delta A^{(III)} = \mu_0 \frac{\partial M}{\partial x} \tag{2}$$

As done in [22], the magnetization can be developed into a Fourier series:

$$M(X_R) = \sum_{n=1}^{+\infty} M_n . \cos\left(n \frac{\pi}{\beta_{a2}\tau} X_R \right) \tag{3}$$

The coefficients M_n are given by:

$$M_n = \frac{4}{\pi} \frac{B_r}{\mu_0} \frac{1}{n} \sin\left(n \frac{\beta_{a_1}}{\beta_{a_2}} \frac{\pi}{2} \right) \tag{4}$$

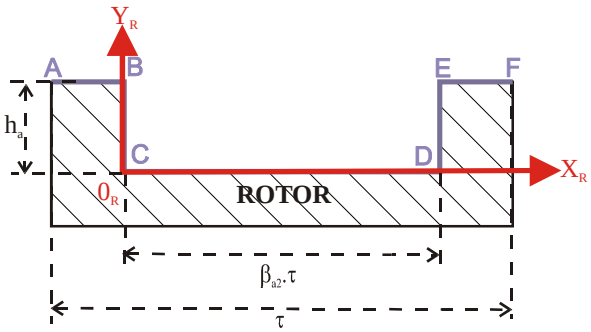

Fig. 4: Zoom on the rotor

It can be shown that the Poisson equation (2), as well as the homogeneous Neumann boundary conditions *dA/dn=0* on the segments [BC], [DE] and [CD] (Fig. 4) are satisfied if the following expression for the potential is chosen, in the main coordinate system *(0xy)*:

$$\begin{aligned} A^{(III)}(x,y) = c_0 + \sum_{n\geq 1} \Bigg[& c_n \cosh\left(n \frac{\pi}{\beta_{a2}\tau} y \right) \\ & - \mu_0 \frac{\beta_{a2}\tau}{\pi} \sum_{n\geq 1} \frac{M_n}{n} \cos\left(n \frac{\pi}{\beta_{a2}\tau} (x - X_d) \right) \Bigg] \\ & \cdot \cos\left(n \frac{\pi}{\beta_{a2}\tau} (x - X_d) \right) \end{aligned} \tag{5}$$

The unknown coefficients c_n ($n \geq 0$) are determined in the next sections.

For Zone II, a Laplace Equation must be solved:

$$\Delta A^{(II)} = 0 \tag{6}$$

Moreover, in this zone, in the airgap (Zone II), an anti-periodicity condition has to be taken into account:

$$A^{(II)}(x+\tau, y) = -A^{(II)}(x,y) \tag{7}$$

This implies that the Fourier series only present odd terms:

$$\begin{aligned} A^{(II)}(x,y) = & \sum_{k\geq 1} b_k(y) \cos\left((2k-1) \frac{\pi}{\tau} x \right) \\ & + \sum_{k\geq 1} b_k'(y) \sin\left((2k-1) \frac{\pi}{\tau} x \right) \end{aligned} \tag{8}$$

The Laplace equation (6) implies:

$$b_k(y) = b_k^{(1)} \cosh\left((2k-1)\frac{\pi}{\tau}y\right) + b_k^{(2)} \sinh\left((2k-1)\frac{\pi}{\tau}y\right)$$
$$b_k'(y) = b_k^{(3)} \cosh\left((2k-1)\frac{\pi}{\tau}y\right) + b_k^{(4)} \sinh\left((2k-1)\frac{\pi}{\tau}y\right) \quad (9)$$

For Zone I, a generic slot *l* is considered, with its local coordinate system $(0_l, X_l, Y_l)$ (Fig. 5).
Due to the currents, the equation in the slot is a Poisson equation:

$$\Delta A^{(I,l)} = -\mu_0 . j_l \quad (10)$$

The homogeneous solution can be found by solving the corresponding Laplace equation ($\Delta A_h^{(I,l)} = 0$):

$$A_h^{(I,l)}(X_l, Y_l) = a_0^{(l)} + \sum_{m\geq 1} a_m^{(l)} \cosh\left(m\frac{\pi}{w_e}(Y_l - h_e)\right)\cos\left(m\frac{\pi}{w_e}X_l\right) \quad (11)$$

A particular solution to the Poisson equation $\Delta A_p^{(I,l)} = -\mu_0 j_l$ must be found. The following quadratic form can be proposed as a particular solution in the slot:

$$A_p^{(I,l)}(X_l, Y_l) = -\frac{1}{2}\mu_0 j_l (Y_l - h_e)^2 \quad (12)$$

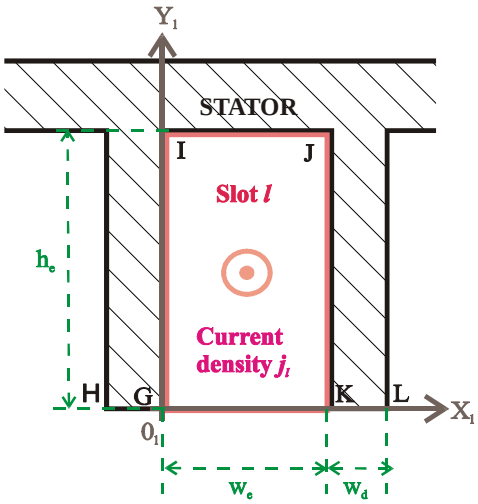

Fig. 5: Zoom on a stator slot

In the main *(0xy)* axis system, it can be found:

$$A^{(I,l)}(x,y) = a_0^{(l)} + \sum_{m\geq 1} a_m^{(l)} \cosh\left(m\frac{\pi}{w_e}\left(y-(h_a+e+h_e)\right)\right)\cos\left(m\frac{\pi}{w_e}\left(x-(l-1)(w_e+w_d)\right)\right) - \frac{1}{2}\mu_0 j_l \left(y-(h_a+e+h_e)\right)^2 \quad (13)$$

C. Boundary conditions between all the different domains

Starting from the mathematical expressions of the previous section, it is possible to write the boundary conditions between all the zones, and determine the series' coefficients. As known in electromagnetic theory, the boundary conditions to satisfy are:

- the continuity of the vector potential
- the continuity of its normal derivative

The following notations are introduced:

- $K_{c_k}^{(II)} = \cosh\left((2k-1)\frac{\pi}{\tau}(h_a+e)\right)$
- $K_{s_k}^{(II)} = \sinh\left((2k-1)\frac{\pi}{\tau}(h_a+e)\right)$

– $K_{c_k}^{(II)\prime} = \cosh\left((2k-1)\frac{\pi}{\tau} h_a \right)$

– $K_{s_k}^{(II)\prime} = \sinh\left((2k-1)\frac{\pi}{\tau} h_a \right)$

– $K_{c_m}^{(I)} = \cosh\left(m\frac{\pi}{w_e} h_e \right)$

– $K_{c_n}^{(III)} = \cosh\left(n\frac{\pi}{\beta_{a2}\tau} h_a \right)$

1) Boundary conditions between Zone I and Zone II.

The continuity of the potential between Zone I and Zone II can be written, in mathematical terms, as:

$$\begin{aligned} &\forall x \in \bigcup_{l=1}^{q_s} \left[(l-1)(w_e + w_d), (l-1)(w_e + w_d) + w_e \right], \\ &A^{(I,l)}\left(x, y = h_a + e\right) = A^{(II)}\left(x, y = h_a + e\right) \end{aligned} \tag{14}$$

Using the boundary integral method explained in [29][30], the following equation can be obtained:

$$\begin{aligned} a_0^{(l)} - \frac{1}{2}\mu_0 j_l h_e^{\,2} = &\sum_{k\geq 1} \left[b_k^{(1)} K_{c_k} + b_k^{(2)} K_{s_k} \right] I_{C,k}^{(l)} \\ &+ \sum_{k\geq 1} \left[b_k^{(3)} K_{c_k} + b_k^{(4)} K_{s_k} \right] I_{S,k}^{(l)} \end{aligned} \tag{15}$$

And, for each slot *l*:

$$\begin{aligned} &\forall m \geq 1, \\ &a_m^{(l)} = \frac{1}{K_{c_m}^{(I)}} \cdot \\ &\left\{ \sum_{k\geq 1} \left[b_k^{(1)} K_{c_k} + b_k^{(2)} K_{s_k} \right] \alpha_{C,(m,k)}^{(l)} + \sum_{k\geq 1} \left[b_k^{(3)} K_{c_k} + b_k^{(4)} K_{s_k} \right] \alpha_{S,(m,k)}^{(l)} \right\} \end{aligned} \tag{16}$$

The normalized coefficients $I_{C,k}^{(l)}$, $I_{S,k}^{(l)}$, $\alpha_{C,(m,k)}^{(l)}$, and $\alpha_{S,(m,k)}^{(l)}$ are given in Appendix II.

Concerning the normal derivative of the potential between Zone I and Zone II, it is possible to write:

$$\begin{aligned} &\forall x \in \bigcup_{l=1}^{q_s} \left[(l-1)(w_e + w_d), (l-1)(w_e + w_d) + w_e \right], \\ &\left(\frac{dA^{(II)}}{dy} \right)_{y = h_a + e} = \left(\frac{dA^{(I)}}{dy} \right)_{y = h_a + e} \\ &\forall x \in [0, \tau] - \left\{ \bigcup_{l=1}^{q_s} \left[(l-1)(w_e + w_d), (l-1)(w_e + w_d) + w_e \right] \right\}, \\ &\left(\frac{dA^{(II)}}{dy} \right)_{y = h_a + e} = 0 \end{aligned} \tag{17}$$

Using again the boundary integral method [29][30], it can be found:

$$\begin{aligned} &\forall k \geq 1 \\ &b_k^{(1)} K_{c_k} - b_k^{(2)} K_{s_k} \\ &= \frac{1}{2k-1} \sum_{l=1}^{q_s} \left\{ -\sum_{m\geq 1} m a_m^{(l)} K_{c_m}^{(I)} \alpha_{C,(m,k)}^{(l)} + 2\frac{\mu_0 h_e w_e j_l}{\pi} I_{C,k}^{(l)} \right\} \end{aligned} \tag{18}$$

And also:

$$\begin{aligned}&\forall k \geq 1\\&b_k^{(3)} K_{c_k} - b_k^{(4)} K_{s_k}\\&= \frac{1}{2k-1} \sum_{l=1}^{q_s} \left\{ -\sum_{m\geq 1} m a_m^{(l)} K_{c_m}^{(I)} \alpha_{S,(m,k)}^{(l)} + 2 \frac{\mu_0 h_e w_e j_l}{\pi} I_{S,k}^{(l)} \right\}\end{aligned} \tag{19}$$

2) Boundary conditions between Zone II and Zone III.

Using the same method as in the previous section for taking into account the boundary conditions, it is possible to get the following relation, for each rotor displacement X_d, for what concerns the potential continuity between Zone II and Zone III:

$$c_0 = \sum_{k\geq 1} \left[b_k^{(1)} K_{c_k}^{(II)\prime} + b_k^{(2)} K_{s_k}^{(II)\prime} \right] J_{C,k} + \sum_{k\geq 1} \left[b_k^{(3)} K_{c_k}^{(II)\prime} + b_k^{(4)} K_{s_k}^{(II)\prime} \right] J_{S,k} \tag{20}$$

And also:

$$\begin{aligned}&\forall n \geq 1,\\&c_n = \frac{1}{K_{c_n}^{(III)}} \cdot \left\{ \sum_{k\geq 1} \left[b_k^{(1)} K_{c_k}^{(II)\prime} + b_k^{(2)} K_{s_k}^{(II)\prime} \right] \beta_{C,(n,k)} \right.\\&\qquad \left. + \sum_{k\geq 1} \left[b_k^{(3)} K_{c_k}^{(II)\prime} + b_k^{(4)} K_{s_k}^{(II)\prime} \right] \beta_{S,(n,k)} - \mu_0 \frac{\beta_{a2}\tau}{\pi} \frac{M_n}{n} \right\}\end{aligned} \tag{21}$$

The definitions and expressions of the normalized numbers $J_{C,k}$, $J_{S,k}$, $\beta_{C,(m,k)}$, and $\beta_{S,(m,k)}$ are given in appendix II.

For the continuity of the normal derivative of the potential between Zones II and III, the two following equations are obtained:

$$\begin{aligned}&\forall k \geq 1\\&b_k^{(1)} K_{c_k}^{(II)\prime} - b_k^{(2)} K_{s_k}^{(II)\prime} = \frac{1}{2k-1} \sum_{n\geq 1} n c_n K_{c_n}^{(III)} \beta_{C,(n,k)}\end{aligned} \tag{22}$$

$$\begin{aligned}&\forall k \geq 1\\&b_k^{(3)} K_{c_k}^{(II)\prime} - b_k^{(4)} K_{s_k}^{(II)\prime} = \frac{1}{2k-1} \sum_{n\geq 1} n c_n K_{c_n}^{(III)} \beta_{S,(n,k)}\end{aligned} \tag{23}$$

D. Solution of the problem.

1) Matrix formulation

All the series are limited to a finite number of terms, called *N*. This number is computed in the next part, so as to offer the best compromise between the computation time, and the accuracy.

The unknown parameters are, using the vector notation:

$$\forall l \in [\![1, q_s]\!], \left[a^{(l)} \right] = \begin{bmatrix} a_1^{(l)} \\ \vdots \\ a_N^{(l)} \end{bmatrix}, \left[b^{(1)} \right] = \begin{bmatrix} b_1^{(1)} \\ \vdots \\ b_N^{(1)} \end{bmatrix}, \left[b^{(2)} \right] = \begin{bmatrix} b_1^{(2)} \\ \vdots \\ b_N^{(2)} \end{bmatrix}, \left[b^{(3)} \right] = \begin{bmatrix} b_1^{(3)} \\ \vdots \\ b_N^{(3)} \end{bmatrix} \left[b^{(4)} \right] = \begin{bmatrix} b_1^{(4)} \\ \vdots \\ b_N^{(4)} \end{bmatrix}, \text{ and } [c] = \begin{bmatrix} c_1 \\ \vdots \\ c_N \end{bmatrix}.$$

Equation (16) can be written for all the numbers *m* between 1 and *N*. So the following matrix equation is obtained, for all slot number *l* between 1 and q_s:

$$\forall l \in [1, q_s], \left[a^{(l)} \right] = [D_1] \left\{ \begin{array}{l} \left[\alpha_C^{(l)} \right] \left([D_2] \left[b^{(1)} \right] + [D_3] \left[b^{(2)} \right] \right) \\ + \left[\alpha_S^{(l)} \right] \left([D_2] \left[b^{(3)} \right] + [D_3] \left[b^{(4)} \right] \right) \end{array} \right\} \tag{24}$$

The following square matrixes for each slot are introduced (see appendix II):

$\left[\alpha_C^{(l)} \right] = \left[\alpha_{C,(m,k)}^{(l)} \right]_{(m,k)\in[1,N]^2}$ and $\left[\alpha_S^{(l)} \right] = \left[\alpha_{S,(m,k)}^{(l)} \right]_{(m,k)\in[1,N]^2}$.

The other diagonal matrixes are also defined in Appendix II.

Equations (18) and (19), for each k between 1 and N, lead to the following matrix relations:

$$[D_2].\left[b^{(1)}\right]-[D_3].\left[b^{(2)}\right]=-[INV]\sum_{l=1}^{q_s}\left[\alpha_C^{(l)}\right]^T[D_4]\left[a^{(l)}\right] + 2\frac{\mu_0 h_e w_e}{\pi}\sum_{l=1}^{q_s} j_l\left[I_C^{(l)}\right] \quad (25)$$

$$[D_2].\left[b^{(3)}\right]-[D_3].\left[b^{(4)}\right]=-[INV]\sum_{l=1}^{q_s}\left[\alpha_S^{(l)}\right]^T[D_4]\left[a^{(l)}\right] + 2\frac{\mu_0 h_e w_e}{\pi}\sum_{l=1}^{q_s} j_l\left[I_S^{(l)}\right] \quad (26)$$

The matrix [*INV*], as well as the following matrixes, are also defined in Appendix II: $\left[I_C^{(l)}\right]=\left[I_{C,k}^{(l)}\right]_{k\in[1,N]}$, and $\left[I_S^{(l)}\right]=\left[I_{S,k}^{(l)}\right]_{k\in[1,N]}$

Thanks to (16), it can be obtained:

$$\forall l\in[1,q_s],\left[a^{(l)}\right]=[D_1]\left\{\left[\alpha_C^{(l)}\right]\left([D_2]\left[b^{(1)}\right]+[D_3]\left[b^{(2)}\right]\right) + \left[\alpha_S^{(l)}\right]\left([D_2]\left[b^{(3)}\right]+[D_3]\left[b^{(4)}\right]\right)\right\} \quad (27)$$

And, from (21):

$$[c]=[D_5]\left\{\left[\beta_C\right]\left([D_6]\left[b^{(1)}\right]+[D_7]\left[b^{(2)}\right]\right) + \left[\beta_S\right]\left([D_6]\left[b^{(3)}\right]+[D_7]\left[b^{(4)}\right]\right)-[V]\right\} \quad (28)$$

The matrix $\left[\beta_C\right]=\left[\beta_{C,(n,k)}\right]_{(n,k)\in[1,N]^2}$ and $\left[\beta_S\right]=\left[\beta_{S,(n,k)}\right]_{(n,k)\in[1,N]^2}$ are also given in Appendix II, as well as the vector $[V]=[V_n]_{n\in[1,N]}$ and the other diagonal matrixes.

Equations (22) and (23) lead to the following matrix equations:

$$[D_6].\left[b^{(1)}\right]-[D_7].\left[b^{(2)}\right]=[INV]\left[\beta_C\right]^T[D_8][c] \quad (29)$$

$$[D_6].\left[b^{(3)}\right]-[D_7].\left[b^{(4)}\right]=[INV]\left[\beta_S\right]^T[D_8][c] \quad (30)$$

2) Numerical computation of the problem.

Recalling the equations' system to solve:

$$\begin{cases} \forall l\in[\![1,q_s]\!],\left[a^{(l)}\right]=[D_1]\left\{\begin{array}{l}\left[\alpha_C^{(l)}\right]\left([D_2]\left[b^{(1)}\right]+[D_3]\left[b^{(2)}\right]\right)\\ +\left[\alpha_S^{(l)}\right]\left([D_2]\left[b^{(3)}\right]+[D_3]\left[b^{(4)}\right]\right)\end{array}\right\} \\ [D_2].\left[b^{(1)}\right]-[D_3].\left[b^{(2)}\right]=-[INV]\sum_{l=1}^{q_s}\left[\alpha_C^{(l)}\right]^T[D_4]\left[a^{(l)}\right]+2\frac{\mu_0 h_e w_e}{\pi}\sum_{l=1}^{q_s} j_l\left[I_C^{(l)}\right] \\ [D_2].\left[b^{(3)}\right]-[D_3].\left[b^{(4)}\right]=-[INV]\sum_{l=1}^{q_s}\left[\alpha_S^{(l)}\right]^T[D_4]\left[a^{(l)}\right]+2\frac{\mu_0 h_e w_e}{\pi}\sum_{l=1}^{q_s} j_l\left[I_S^{(l)}\right] \\ [c]=[D_5]\left\{\left[\beta_C\right]\left([D_6]\left[b^{(1)}\right]+[D_7]\left[b^{(2)}\right]\right)+\left[\beta_S\right]\left([D_6]\left[b^{(3)}\right]+[D_7]\left[b^{(4)}\right]\right)-[V]\right\} \\ [D_6].\left[b^{(1)}\right]-[D_7].\left[b^{(2)}\right]=[INV]\left[\beta_C\right]^T[D_8][c] \\ [D_6].\left[b^{(3)}\right]-[D_7].\left[b^{(4)}\right]=[INV]\left[\beta_S\right]^T[D_8][c] \end{cases} \quad (31)$$

If q_s=3, a system of 8 equations with 8 unknown vectors must be solved. Equations (25) and (26) are substituted in Equation (24). In order to reduce the number of equations, the following process is proposed: in a first stage, by an analytical substitution, we can express this system with only the unknown series' coefficients vectors: $[b^{(1)}][b^{(2)}][b^{(3)}][b^{(4)}]$. After algebraic substitutions, the system can be written under the form:

$$[M].[b]=[P] \qquad (32)$$

Where the unknown vector [b] is $[b]=\begin{bmatrix}[b^{(1)}]\\ [b^{(2)}]\\ [b^{(3)}]\\ [b^{(4)}]\end{bmatrix}$. The matrix [M] and the vector [P] are obtained by linear combinations of the matrixes introduced in the previous section.

To solve the linear system (32), it is necessary to perform a numerical inversion of the matrix [M]. It is also necessary to choose the number N of harmonics. For that, the following numerical procedure may be proposed: firstly, it is possible to compute the inversion of the system for N=1, which is very fast, since the size of the matrix [M] is just 4. Then the following algorithm is applied.

Suppose that we have just computed the solution for a certain number N of harmonics. For this number, the matrix [M] is called $[M_N]$, [V] is called $[V_N]$, and the solution $[b_N]$ is:

$$[b_N]=\left[\left[b_N^{(1)}\right]^T \quad \left[b_N^{(2)}\right]^T \quad \left[b_N^{(3)}\right]^T \quad \left[b_N^{(4)}\right]^T\right]^T$$

To compute the vector solution $[b_{N+1}]$ for N+1 harmonics, which is solution of the equation $[M_{N+1}].[b_{N+1}]=[V_{N+1}]$, a Gauss-Siedel algorithm can be used. In this inversion method, a first initialisation of the solution is required. Instead of taking the zero vector for the initialisation, we use in the initial step the solution of the previous system with N harmonics, more precisely:

$$[b_{N+1,0}]=\left[\left[b_N^{(1)}\right]^T 0 \quad \left[b_N^{(2)}\right]^T 0 \quad \left[b_N^{(3)}\right]^T 0 \quad \left[b_N^{(4)}\right]^T 0\right]^T$$

So the number of iterations of the Gauss-Seidel process is reduced in order to get the solution $[b_{N+1}]$. We stop increasing the number N when the difference of the solutions between two iterations becomes as small as wanted (in practice less than 1% in relative value). So the number N of harmonics is not fixed, but is optimized for each machine's geometry.

V. COMPARISON WITH FINITE ELEMENTS

For the finite element verification, as well as for the torque computations, the geometry presented in Table II is used. Moreover, for the torque computations, the mean airgap radius (i.e. the mid airgap radius R_m of the radial flux machine, or the mean active radius of the axial flux machine) is assumed to be 0.1m (see Appendix I for a detailed discussion about this point). In the finite element code, in order to be consistent with the assumption of infinite iron permeability made for the analytical model, a high relative permeability is assigned to the ferromagnetic parts (in practice, this relative permeability is taken equal to 1000). A discussion about the consequences of this linear model is provided in Appendix I: the results are compared with ones obtained using non linear B-H experimental relationships.

TABLE II
GEOMETRY OF THE MACHINE CHOSEN FOR THE INDUCTION AND TORQUE COMPUTATIONS (ANALYTICAL AND FINITE ELEMENT VERIFICATION)

Notation	Numerical values
h_a	5mm
e	2mm
e_{cr}	10mm
e_{cs}	10mm
h_e	30mm
τ	60mm
β_{a1}	0.6
β_{a2}	0.8
w_e	10mm
w_d	10mm
H	100mm
B_r	1.2T

A. The magnets' field.

The no-load airgap magnetic field (created by the magnets, when all the stator currents are zero) has been computed, both analytically and by finite elements. On Fig. 6, a contour [AB] in the middle of the airgap is chosen, on which we shall plot the induction caused by the magnets (all the current densities $j_1=j_2=j_3=0$). This segment length is equal to the pole pitch τ. The results are shown on Fig. 7, Fig. 8 and Fig. 9, respectively for the potential, the B_x and the B_y induction components. The agreement is satisfying.

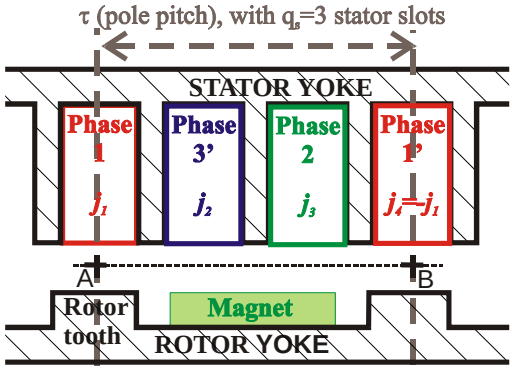

Fig. 6: The plot contour [AB] in the airgap

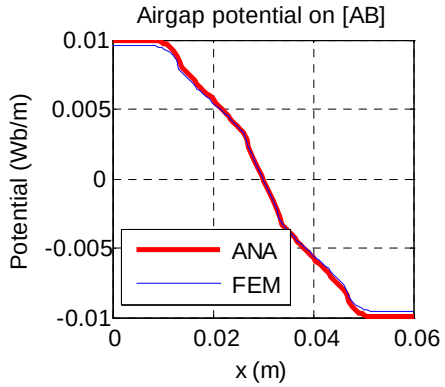

Fig. 7: The potential caused by the magnets on the segment [AB]

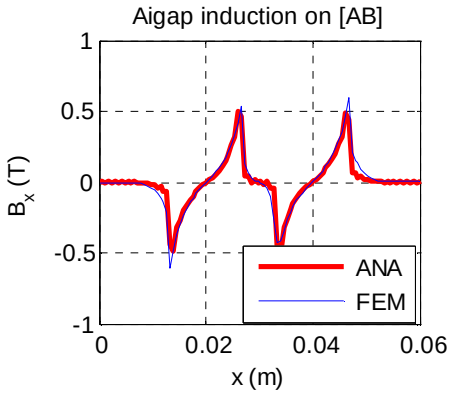

Fig. 8: The B_x induction caused by the magnets on the segment [AB]

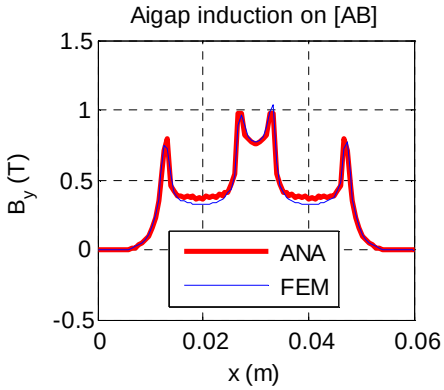

Fig. 9: The B_y induction caused by the magnets on the segment [AB]

B. The stator currents'field.

The results of the field caused by the stator currents (in the computation procedure, B_r=0) are now analyzed. According to the Park theory, a *d* axis current is applied. Since the system is linear, the calculus is performed for a current of just 1A in each slot. So, on Fig. 6, current densities of $j_1=1A/S_{slot}$ (S_{slot} is the slot surface), $j_2=j_1/2$, and, $j_3=-j_1/2$ have been applied. For the *q* axis current, the rotor undergoes a translation of a half pole pitch in comparison with the *d* axis calculation. The results for the *d* axis currents are shown on Fig. 10, Fig. 11 and Fig. 12, in good accordance with finite elements.

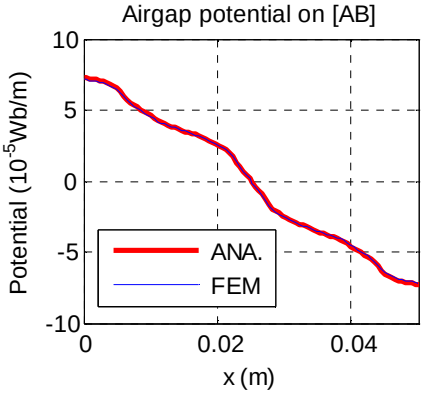

Fig. 10: The potential caused by the d axis currents on the segment [AB]

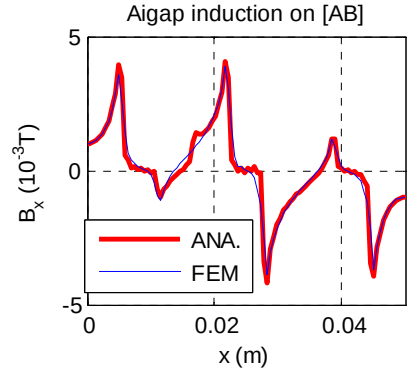

Fig. 11: The B_x induction caused by the d axis currents on [AB]

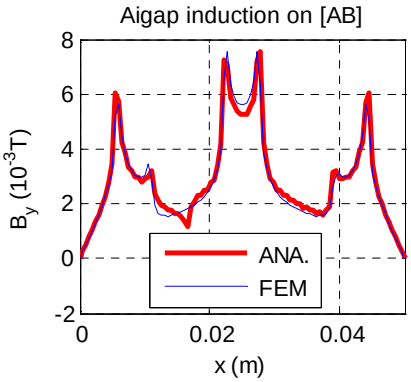

Fig. 12: The B_y induction caused by the d axis currents on [AB]

The results obtained using the two methods are in good agreement. The time necessary for the analytical computation is about 30% less than the time necessary for the finite element calculation.

VI. THE INSTANTANEOUS TORQUE COMPUTATION

A. The calculation method

The analytical model can be used for the computation of the instantaneous torque. The analytical computation is performed as the following: the Maxwell stress tensor formula is applied on the [AB] segment of Fig. 6 located in the middle of the airgap, giving the tangential effort on this segment as:

$$F_t = \int_{[AB]} H_x B_y dx \qquad (33)$$

This analytical calculation is repeated for each elementary position of the rotor.
The torque calculation with finite elements is based on the same principles, but the field and induction and then the Maxwell stress tensor are computed numerically on the [AB] segment. The spatial period of the torque is a tooth pitch. The tooth pitch has been decomposed in ten elementary positions (both for finite element or analytical computation). For each of them, the calculation has been carried out, and a cubic interpolation has been applied between the ten points. This strategy permits to save computation time, without decreasing the model accuracy.
In the Park formalism, a *q* current of 800A per slot and a *d* current per slot of -100A are applied. The total torque is shown on Fig. 13. The analytical and finite elements calculations are in good agreement: the mean torque is around 170Nm for the two methods.

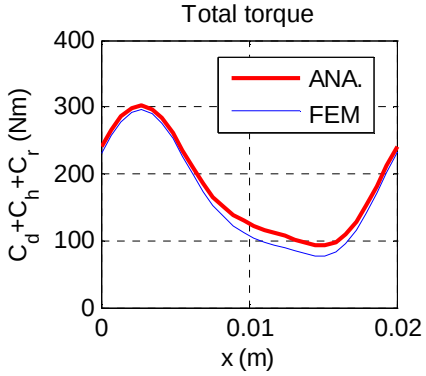

Fig. 13: The total torque over a tooth pich

The cogging torque is given on Fig. 14, (it is computed with zero currents). Its mean value is zero (as expected), although its variations are quite high (50Nm). The discrepancy of 8% on the maximum value can be explained by the fact that the instantaneous torque computation is very sensitive to the number *N* of harmonics chosen for the analytical computation. Indeed, the torque is obtained by multiplying two derivatives of the potential: the normal induction B_y and the tangential field $H_x=B_x/\mu_0$. These derivatives are quite irregular signals (see the previous section), and an important number of harmonics can be required to represent them with a good precision. Here, as explained in Section IV.D.2, we stopped increasing the number *N* of harmonics if the [b] vectors between two iterations do not present more than 1% of difference in relative value. If we choose a lowest error, the torques computed by finite elements and analytically become closer (a difference of 4% is observed for a relative error of 0.3%). However, this solution does not appear as optimal, because it increases much the computation time, and then cannot be used for a pre-design process. We believe that a

difference of about 10% is acceptable in a pre-design process stage. The most important is however to get an exact mean value, which is the case, even for a small number of harmonics.

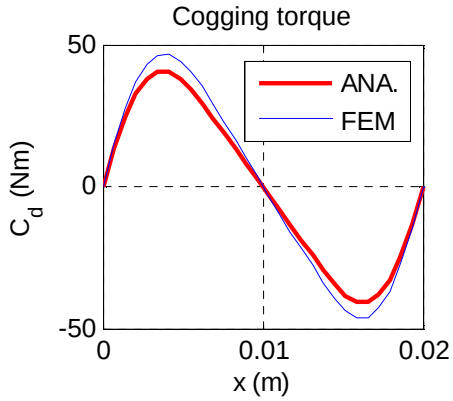

Fig. 14: The cogging torque over a tooth pich

The reluctant torque, which is due only to the stator currents (the remanent induction of the magnets is put to zero), is presented in Fig. 15. The fluctuation is quite important, but the mean value remain weak (10Nm) compared to the total torque, mainly due to the hybrid torque component. This one is obtained by subtracting to the total torque the cogging and the reluctant torque (Fig. 16).

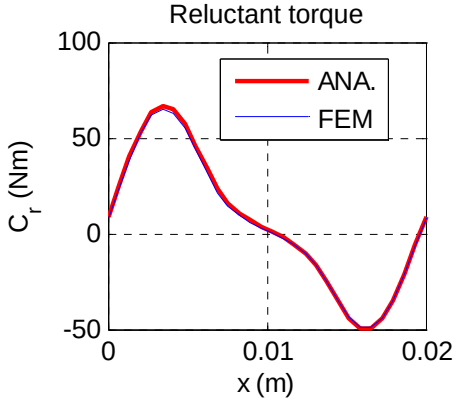

Fig. 15: The reluctant torque over a tooth pich

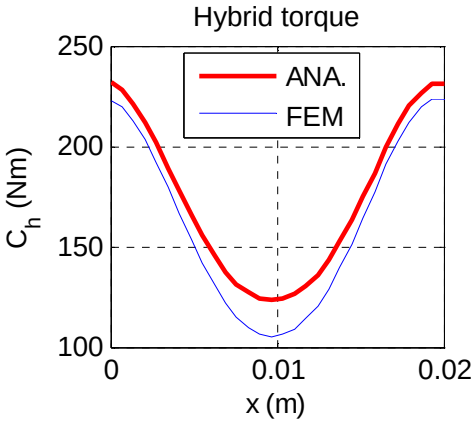

Fig. 16: The hybrid torque over a tooth pich

B. Discussion

It has been shown that the analytical method gives results in good agreement with finite elements. Nevertheless, it could be interesting to illustrate the limit of this method.

The main limit of the method consists in the fact that saturation of the machine's ferromagnetic parts is not taken into account. So torque calculations are performed in this section using the finite element method including ferromagnetic material saturation (the FeSi B-H curve given in Appendix I), and the results are compared with the analytical model. This calculation permits to understand the consequences of this limitation on the torque computation.

So a high *q* axis current (up to 500A) is applied, so as to create saturation, and this case is studied using finite elements computations. The mean torque is computed over a tooth pitch, as in the previous section. The torque curve taking into account saturation is compared with the one derived from our analytical linear model. This work has been done for two values of *d* axis current. The first is for a zero *d* axis current (Fig. 17), and the second is for a *d* axis current per slot of nI_d=-600A (Fig. 18).
The first fact to notice is that the saturation phenomena reduces the total flux in the machine, especially when the *q* axis current is high Therefore the torque is not as high as in the non saturated case.
Another point is the effect of the *d* axis current. A strong *d* axis current permits to increase the torque significantly, since it allows a reluctant torque component. But it also permits a reduction of the effect of saturation (Fig. 18), because the total flux of the machine is weakened. It could be shown in the same way that flux weakening also decreases the iron losses.

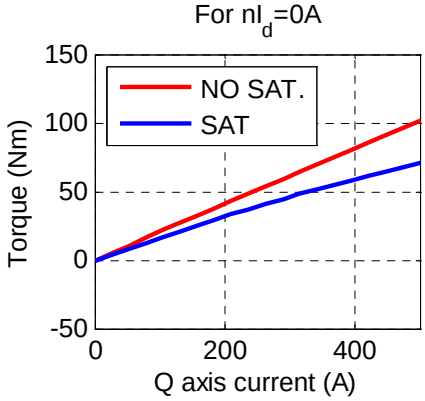

Fig. 17: Mean torque with and without saturation (nI_d=0)

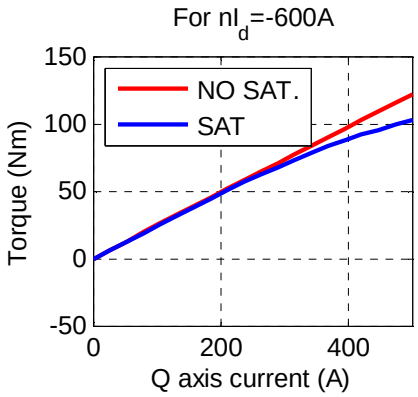

Fig. 18: Mean torque with and without saturation (nI_d=-600A)

VII. Conclusion

An analytical method was developed in order to take into account the stator and rotor saliency of the machine, for the computation of the magnetic induction in the machine airgap. This permits to compute precisely the machine's torque. In a coming paper, we are going to use this model for the computation of the inductions in the ferromagnetic parts of the machine, so as to be able to evaluate the iron losses, taking into account the stator leakage flux.

References

[1] A. Wang, Y. Jia, and W.L. Soong, "Comparison of Five Topologies for an Interior Permanent-Magnet Machine for a Hybrid Electric Vehicle," *IEEE Transactions on Magnetics*, vol. 47, no. 10, 2011.

[2] E. Sulaiman, T. Kosaka, and N. Matsui, "High Power Density Design of 6-Slot--8-Pole Hybrid Excitation Flux Switching Machine for Hybrid Electric Vehicles," *IEEE Transactions on Magnetics*, vol. 47, no. 10, pp. 4453-4456, 2011.

[3] T. Arakawa et al., "Examination of an Interior Permanent Magnet Type Axial Gap Motor for the Hybrid Electric Vehicle," *IEEE Transactions on Magnetics*, vol. 47, no. 10, pp. 3602-3605, 2011.

[4] J. Kwack, S. Min, and J.P. Hong, "Optimal stator design of interior permanent magnet motor to reduce torque ripple using the level set method," *IEEE Transactions on Magnetics*, vol. 46, no. 10, pp. 2108-2111, 2006.

[5] S. Javadi and M. Mirsalim, "Design and analysis of 42-V coreless axial-flux permanent-magnet generators for automotive applications," *IEEE Transactions on Magnetics*, vol. 46, no. 4, pp. 1015-1023, 2010.

[6] M. Ashabani and Y. Mohamed, "Multiobjective shape optimization of segmented pole permanent-magnet synchronous machines with improved torque characteristics," *IEEE Transactions on Magnetics*, vol. 47, no. 4, pp. 795-804, 2011.

[7] Y. Liu et al., "Optimization of an 80 kW Radial-Radial Flux Compound-Structure Permanent-Magnet Synchronous Machine Used for HEVs," *IEEE Transactions on Magnetics*, vol. 47, no. 10, pp. 2399-2402, 2011.

[8] J. Kwack, S. Min, and J.P. Hong, "Optimal stator design of interior permanent magnet motor to reduce torque ripple using the level set method," *IEEE Transactions on Magnetics*, vol. 46, no. 6, pp. 2108-2111, 2010.

[9] L. Fang, S.I. Kim, S.O. Kwon, and J.P. Hong, "Novel double-barrier rotor designs in interior-PM motor for reducing torque pulsation," *IEEE Transactions on Magnetics*, vol. 46, no. 6, pp. 2183-2186, 2010.

[10] J.C. Urresty, J.R. Riba, L. Romeral, and A. Garcia, "A Simple 2-D Finite-Element Geometry for Analyzing Surface-Mounted Synchronous Machines With Skewed Rotor Magnets," *IEEE Transactions on Magnetics*, vol. 46, no. 11, pp. 3948-3954, 2010.

[11] J. Li, K.T. Chau, J.Z. Jiang, C. Liu, and W. Li, "A new efficient permanent-magnet vernier machine for wind power generation," *IEEE Transactions on Magnetics*, vol. 46, no. 6, pp. 1475-1478, 2010.

[12] D. Zarko, D. Ban, and T.A. Lipo, "Analytical solution for cogging torque in surface permanent-magnet motors using conformal mapping," *IEEE Transactions on Magnetics*, vol. 44, no. 1, pp. 52-65, 2008.

[13] Z.Q. Zhu, L.J. Wu, and Z.P. Xia, "An accurate subdomain model for magnetic field computation in slotted surface-mounted permanent-magnet machines," *IEEE Transactions on Magnetics*, vol. 44, no. 6, pp. 1100-1115, 2010.

[14] W. Xu, J. Zhu, Y. Zhang, Y. Guo, and G. Lei, "New Axial Laminated-Structure Flux-Switching Permanent Magnet Machine With 6/7 Poles," *IEEE Transactions on Magnetics*, vol. 47, no. 10, pp. 2823-2826, 2011.

[15] Z.Q. Zhu and D. Howe, "Instantaneous magnetic field distribution in brushless permanent magnet DC motors. III. Effect of stator slotting," *IEEE Transactions on Magnetics*, vol. 29, no. 1, pp. 143-151, 1993.

[16] F.W. Carter, "Air-gap induction," *Electrical world and engineering*, vol. 38, no. 22, pp. 884-888, 1901.

[17] B.L.J. Gysen, E. Ilhan, K.J. Meessen, J.J.H. Paulides, and E.A. Lomonova, "Modeling of flux switching permanent magnet machines with Fourier analysis," *IEEE Transactions on Magnetics*, vol. 46, no. 6, pp. 1499-1502, 2010.

[18] M. Markovic, M. Jufer, and Y. Perriard, "Determination of tooth cogging force in a hard-disk brushless DC motor," *IEEE Transactions on Magnetics*, vol. 41, no. 12, pp. 4421-4426, 2005.

[19] K. Boughrara, D. Zarko, R. Ibtiouen, O. Touhami, and A. Rezzoug, "Magnetic Field Analysis of Inset and Surface-Mounted Permanent-Magnet Synchronous Motors Using Schwarz--Christoffel Transformation," *IEEE Transactions on Magnetics*, vol. 45, no. 8, pp. 3166-3178, 2009.

[20] "Numerical conformal mapping using cross-ratio and Delaunay triangulation," *SIAM J. Sci. Comput.*, vol. 19, pp. 1783–1803, 1998.

[21] A. Rahideh and T. Korakianitis, "Analytical magnetic field distribution of slotless brushless machines with inset permanent magnets," *IEEE Transactions on Magnetics*, vol. 47, no. 6, pp. 1763-1774, 2011.

[22] O. de la Barrière, H. Ben Ahmed, M. Gabsi, and M. LoBue, "Two-dimensional analytical field model of an inset permanent synchronous machine," *Electromotion*, vol. 17, pp. 81-90, 2010.

[23] T. Lubin, S. Mezani, and A. Rezzoug, "Exact analytical method for magnetic field computation in the air gap of cylindrical electrical machines considering slotting effects," *IEEE Transactions on Magnetics*, vol. 46, no. 4, pp. 1092-1099, 2010.

[24] H. Bali, Y. Amara, G. Barakat, R. Ibtiouen, and M. Gabsi, "Analytical modeling of open circuit magnetic field in wound field and series double excitation synchronous machines," *IEEE Transactions on Magnetics*, vol. 46, no. 10, pp. 3802-3815, 2010.

[25] T. Lubin, S. Mezani, and A. Rezzoug, "2D exact analytical model for surface-mounted permanent-magnet motors with semi-closed slots," *IEEE Transactions on Magnetism*, vol. 47, no. 2, pp. 479-492, 2011.

[26] S.M. Lukic and A. Emadi, "Effects of drivetrain hybridization on fuel economy and dynamic performance of parallel hybrid electric vehicles," *IEEE Transactions on Vehicular Technology*, vol. 53, no. 2, pp. 385-389, 2004.

[27] O. de la Barriere, H. Ben Ahmed, and M. Gabsi, "Axial flux machine design for hybrid traction applications," in *4th IET Conference on Power Electronics, Machines and Drives (PEMD)*, York, 2008, pp. 174-178.

[28] F. Marignetti, V.D. Colli, and S. Carbone, "Comparison of axial flux PM synchronous machines with different rotor back cores," *IEEE Transactions on Magnetics*, vol. 46, no. 2, pp. 598-601, 2010.

[29] F. M. Sargos and A. Rezzoug, "Calcul analytique du champ engendré par des aimants dans l'entrefer d'une machine à rotor denté," *Journal de Physique III*, vol. 1, pp. 103-110, 1991.

[30] F. Dubas and C. Espanet, "Analytical Solution of the Magnetic Field in Permanent-Magnet Motors Taking Into Account Slotting Effect: No-Load Vector Potential and Flux Density Calculation," *IEEE Transactions on Magnetics*, vol. 45, no. 5, pp. 2097-2109, 2009.

[31] N. Boules, "Two-Dimensional Field Analysis of Cylindrical Machines with Permanent Magnet Excitation," *IEEE Transactions on Industry Applications*, vol. IA-20, no. 5, pp. 1267-1277, 1984.

APPENDIX 1

In this appendix, the two fundamental simplifying assumptions of this work (no curvature effect, no saturation) are discussed.

A. The curvature effect

It is possible to use the model presented in this article for a radial flux machine, on the condition of neglecting the curvature effect. It means that the real machine is made equivalent to a linear actuator, as shown in Fig. 19. The pole pitch τ of the linear actuator is chosen equal to the pole pitch of the radial flux machine at is mean airgap radius R_m (i.e. the mid airgap radius). All the other radial dimensions (magnet thickness h_a, airgap width e, slot dept h_e…) are the same for both actuators. The relative magnet opening on the pole pitch and the relative slot opening on the tooth pitch are also identical.

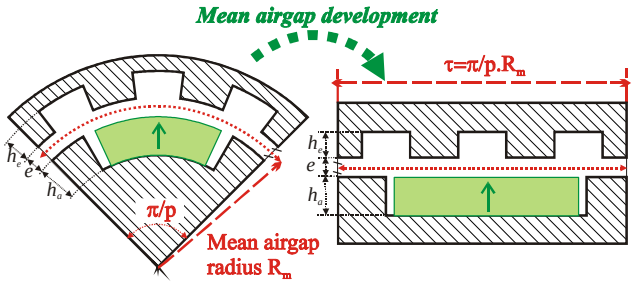

Fig. 19: Development of the radial flux machine to its mean radius to obtain the equivalent linear actuator

This approximation is justified if the mean airgap radius R_m is important compared to the other radial dimensions (magnet thickness, airgap width, slot dept…). To understand to what extend the approximation can be done, finite element calculations have been carried out with the radial flux machine, and with the equivalent linear actuator, in order to compare the results. The machine geometry used in the comparison is given in Table III. The ferromagnetic parts are taken into account using a linear material of relative magnetic permeability equal to 1000.

TABLE III
GEOMETRICAL PARAMETERS OF THE RADIAL FLUX MACHINE

Description	Notation	Numerical value
Dimensions along the radial direction		
Mean airgap radius	R_m	0.076m
Airgap width	e	0.002m
Slot dept	h_e	0.03m
Magnet thickness	h_a	Interval [0.001m;0.01m]
Dimensions along the orthoradial direction		
Pole pair number	p	4
Pole pitch	τ	0.06m
Magnet relative opening with regard to the pole pitch	β_{a1} ($0<\beta_{a1}<1$)	0.6
Rotor inter-teeth space relative opening with regard to the pole pitch	β_{a2} ($\beta_{a1}<\beta_{a2}<1$)	0.8
Stator relative slot opening with regard to the tooth pitch	β_e ($0<\beta_e<1$)	0.5
Dimensions along the *z* direction		
Active thickness of the machine along the *z* axis	H	0.1m
Physical data		
Remanent induction of the magnets (*NdFeB*) at room temperature	B_r	1.2T

For example, the no-load flux is studied. The parameter of importance is the value of the ratio h_a/R_m between the magnet radial thickness and the mean airgap radius. The magnet thickness varies between 0.001m and 0.01m. The ratio between the no-load flux of the two actuators is shown in Fig. 20.

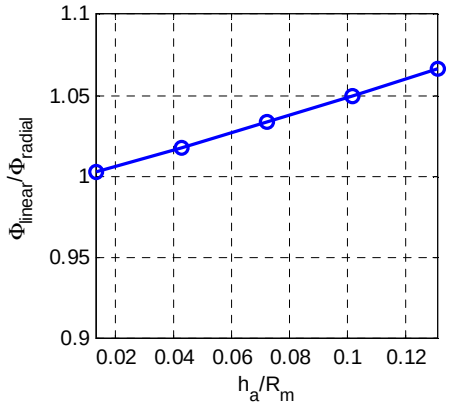

Fig. 20: Ratio between the no-load fluxes obtained in the radial flux machine and the equivalent linear machine

As expected, the two fluxes are nearly the same for small magnet thicknesses with regard to the pole pitch, whereas some discrepancy appears by increasing the magnet thickness. However, the difference is never more than 7% in relative value. Moreover, a magnet thickness of 0.01m (for which the difference is the highest) is not useful, because, as shown in Fig. 21, no significant increase of the

no-load flux appears between the two last points of the magnet thicknesses. Thus it can be concluded that the error on the no-load flux made by the development of the radial flux machine to the equivalent linear one is restricted to a few percent in relative value. However, if this error has to be corrected, some authors have proposed methods based on conformal mapping [29], in order to rigorously transform the radial flux machine to an equivalent linear actuator. This conclusion allows us to compute the magnetic field in the linear equivalent actuator (in Cartesian coordinates), and then apply the results to the case of the radial flux machine.

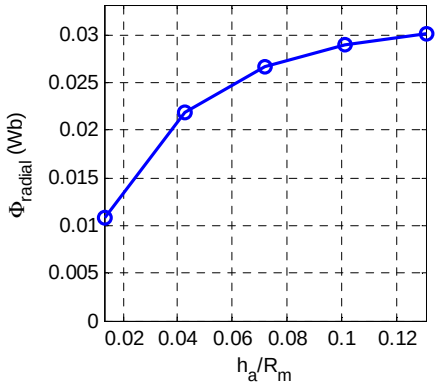

Fig. 21: No-load flux in the radial flux machine (in function of the magnet thickness h_a)

It can also be useful to check if the inductions are locally also the same for the two kinds of machines. For that, it is proposed to plot in Fig. 22 and Fig. 23 the normal and the tangential inductions in the middle of the airgap (dotted red line in Fig. 19). Indeed these inductions are involved in the cogging torque computation, and of course in the no-load flux calculation (the no-load flux is the integral of the normal induction component). It can be seen that the waveforms are nearly identical, which demonstrates the validity of the mean radius development also for the local induction computation.

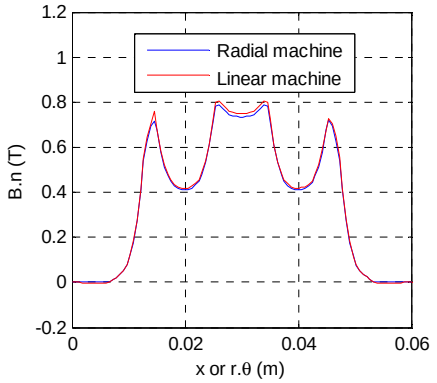

Fig. 22: No-load induction (normal component) in the radial flux machine and in the equivalent linear one (for a magnet thickness h_a=0.0035m) on a line located in the middle of the airgap (dotted red line of Fig. 19)

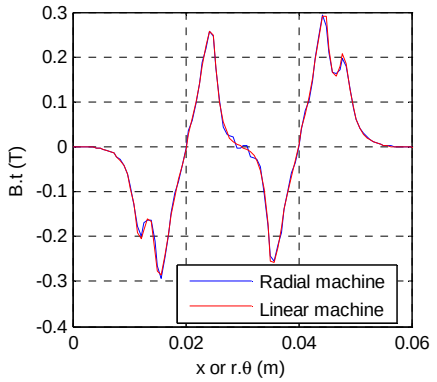

Fig. 23: No-load induction (tangential component) in the radial flux machine and in the equivalent linear one (for a magnet thickness h_a=0.0035m) on a line located in the middle of the airgap (dotted red line of Fig. 19)

B. The saturation effect

The analytical model implies that the ferromagnetic parts are assumed to have an infinite magnetic permeability. It is appropriate to compare the results provided by this model with the ones obtained with real non-linear B-H anhysteretic relationships experimentally measured in Iron-Silicon (FeSi) and Iron-Cobalt (FeCo) laminations (Fig. 24). The main advantage of Iron-Cobalt material is its high

saturation magnetization (nearly 2.3T), and high initial permeability. Its drawback is its high cost and low resistivity, which implies high dynamic loss. The computations are then carried out using a non-linear finite element code.

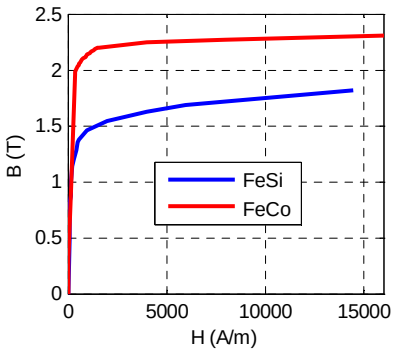

Fig. 24: Non-linear B-H anhysteretic relationships experimentally obtained in FeSi and FeCo laminations

In this study, the same geometry as in Table II is adopted. The B_y inductions obtained on the [AB] segment (Fig. 6), using the analytical and the non-linear finite element models, are plotted in Fig. 25 for no-load excitation conditions. The analytical model and the non-linear finite element model with the FeCo curve provide identical results, while a decrease of the airgap induction can be seen with the FeSi material. This decrease is responsible of an error of 8% on the total no-load flux between the analytical model, and the model using the FeSi curve.

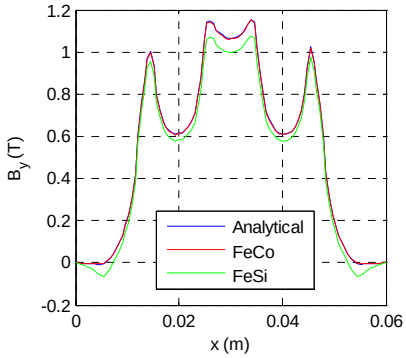

Fig. 25: B_y induction obtained on the [AB] segment (Fig. **6**) for the analytical model, and the non-linear finite element models using the FeCo material and the FeSi material (no-load excitation conditions)

In Fig. 26, the same analysis has been repeated, being this time under field weakening conditions: in addition to the magnets' field, a *d* axis current has been added (nI_d=-600A/m, see Section VI.B). The level and the waveform shape has been changed compared to the previous case in which only the no-load flux was considered. It is interesting to notice that the field weakening permits to reduce the saturation level of the machine, and then justify the use of the linear analytical model. Indeed the difference on the fluxes between the linear model and the FeSi saturated model is now 3% in relative value, whereas it was 8% under no-load condition.

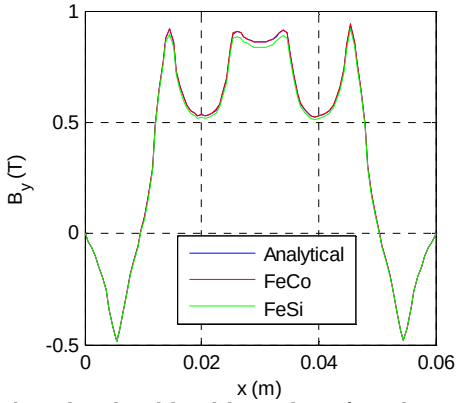

Fig. 26: B_y induction obtained on the [AB] segment for the analytical model, and the non-linear finite element models using the FeCo material and the FeSi material (field weakening condition: superposition of the magnets' field and *d* axis current nI_d=-600A/m)

To conclude, it must be said that the saturation effect can decrease the airgap induction level, and then the torque (see Section VI for a detailed discussion). The flux weakening reduces the saturation effect. However, for the studied geometry, this effect is limited to a decrease of 10% of the airgap induction between the analytical model and the non-linear model using FeSi laminations. For FeCo laminations, due to the very high saturation level of this material, the saturation do not need to be taken into account, justifying the use of the analytical model.

It must be noticed that the saturation effect can be taken into account using the model proposed by the author of [31]. The decrease of the airgap induction due to the saturation effect is modeled by a fictitious increase of the airgap thickness in the analytical computations.

APPENDIX 2

The numbers α introduced in for the continuity conditions were defined the formulas:

$$\alpha_{C,(m,k)}^{(l)} = \sin_C\left(\pi\frac{m\tau-(2k-1)w_e}{2\tau}\right)\cos\left(\pi\frac{m\tau-(2k-1)w_e}{w_e\tau}(l-1)(w_e+w_d)-\frac{m\pi(l-1)(w_e+w_d)}{w_e}+\pi\frac{m\tau-(2k-1)w_e}{2\tau}\right) + \sin_C\left(\pi\frac{m\tau+(2k-1)w_e}{2\tau}\right)\cos\left(\pi\frac{m\tau+(2k-1)w_e}{w_e\tau}(l-1)(w_e+w_d)-\frac{m\pi(l-1)(w_e+w_d)}{w_e}+\pi\frac{m\tau+(2k-1)w_e}{2\tau}\right) \quad (34)$$

$$\alpha_{S,(m,k)}^{(l)} = \sin_C\left(\pi\frac{m\tau+(2k-1)w_e}{2\tau}\right)\sin\left(\pi\frac{m\tau+(2k-1)w_e}{w_e\tau}(l-1)(w_e+w_d)-\frac{m\pi(l-1)(w_e+w_d)}{w_e}+\pi\frac{m\tau+(2k-1)w_e}{2\tau}\right) - \sin_C\left(\pi\frac{m\tau-(2k-1)w_e}{2\tau}\right)\sin\left(\pi\frac{m\tau-(2k-1)w_e}{w_e\tau}(l-1)(w_e+w_d)-\frac{m\pi(l-1)(w_e+w_d)}{w_e}+\pi\frac{m\tau-(2k-1)w_e}{2\tau}\right) \quad (35)$$

$$I_{S,k}^{(l)} = \sin_C\left((2k-1)\frac{\pi}{2\tau}w_e\right)\sin\left((2k-1)\frac{\pi}{\tau}(l-1)(w_e+w_d)+(2k-1)\frac{\pi}{2\tau}w_e\right) \quad (36)$$

$$I_{C,k}^{(l)} = \sin_C\left((2k-1)\frac{\pi}{2\tau}w_e\right)\cos\left((2k-1)\frac{\pi}{\tau}(l-1)(w_e+w_d)+(2k-1)\frac{\pi}{2\tau}w_e\right) \quad (37)$$

The different normalized coefficients for the potential continuity equalities between Zone I and Zone II are given by:

$$J_{C,k} = \sin_C\left((2k-1)\beta_{a2}\frac{\pi}{2}\right)\cos\left((2k-1)\frac{\pi}{\tau}X_d+(2k-1)\beta_{a2}\frac{\pi}{2}\right) \quad (38)$$

$$J_{S,k} = \sin_C\left((2k-1)\beta_{a2}\frac{\pi}{2}\right)\sin\left((2k-1)\frac{\pi}{\tau}X_d+(2k-1)\beta_{a2}\frac{\pi}{2}\right) \quad (39)$$

$$\beta_{C,(n,k)} = \sin_C\left[(n-(2k-1)\beta_{a2})\frac{\pi}{2}\right]\cos\left(\pi\frac{n-(2k-1)\beta_{a2}}{\beta_{a2}\tau}X_d-\frac{n\pi X_d}{\beta_{a2}\tau}+(n-(2k-1)\beta_{a2})\frac{\pi}{2}\right)+\sin_C\left[(n+(2k-1)\beta_{a2})\frac{\pi}{2}\right]\cos\left(\pi\frac{n+(2k-1)\beta_{a2}}{\beta_{a2}\tau}X_d-\frac{n\pi X_d}{\beta_{a2}\tau}+(n+(2k-1)\beta_{a2})\frac{\pi}{2}\right) \quad (40)$$

$$\beta_{S,(n,k)} = \sin_C\left[(n+(2k-1)\beta_{a2})\frac{\pi}{2}\right]\sin\left(\pi\frac{n+(2k-1)\beta_{a2}}{\beta_{a2}\tau}X_d-\frac{n\pi X_d}{\beta_{a2}\tau}+(n+(2k-1)\beta_{a2})\frac{\pi}{2}\right)-\sin_C\left[(n-(2k-1)\beta_{a2})\frac{\pi}{2}\right]\sin\left(\pi\frac{n-(2k-1)\beta_{a2}}{\beta_{a2}\tau}X_d-\frac{n\pi X_d}{\beta_{a2}\tau}+(n-(2k-1)\beta_{a2})\frac{\pi}{2}\right) \quad (41)$$

$$V_n = \mu_0\frac{\beta_{a2}\tau}{\pi}\frac{M_n}{n} \quad (42)$$

When the equations are put under a matrix formulation, it is convenient to introduce the following diagonal matrix:

$$[D_1]=\begin{bmatrix}\ddots & & \\ & \dfrac{1}{\cosh\left(m\frac{\pi}{w_e}h_e\right)} & \\ & & \ddots\end{bmatrix},\ [D_2]=\begin{bmatrix}\ddots & & \\ & \cosh\left((2k-1)\frac{\pi}{\tau}(h_a+e)\right) & \\ & & \ddots\end{bmatrix}\ [D_3]=\begin{bmatrix}\ddots & & \\ & \sinh\left((2k-1)\frac{\pi}{\tau}(h_a+e)\right) & \\ & & \ddots\end{bmatrix},$$

396 $$[D_4]=\begin{bmatrix}\ddots & & \\ & m\cosh\left(m\frac{\pi}{w_e}h_e\right) & \\ & & \ddots\end{bmatrix},\ [INV]=\begin{bmatrix}\ddots & & \\ & \frac{1}{2k-1} & \\ & & \ddots\end{bmatrix},\ [D_5]=\begin{bmatrix}\ddots & & \\ & \frac{1}{\cosh\left(n\frac{\pi}{\beta_{a2}\tau}h_a\right)} & \\ & & \ddots\end{bmatrix},$$

397 $$[D_6]=\begin{bmatrix}\ddots & & \\ & \cosh\left((2k-1)\frac{\pi}{\tau}h_a\right) & \\ & & \ddots\end{bmatrix},\ \text{and}\ [D_7]=\begin{bmatrix}\ddots & & \\ & \sinh\left((2k-1)\frac{\pi}{\tau}h_a\right) & \\ & & \ddots\end{bmatrix},\ [D_8]=\begin{bmatrix}\ddots & & \\ & n\cosh\left(n\frac{\pi}{\beta_{a2}\tau}h_a\right) & \\ & & \ddots\end{bmatrix}.$$